Revealing capacitive and inductive effects in modern industrial c-Si photovoltaic cells through impedance spectroscopy

van Nijen, David A.; Muttillo, Mirco; Van Dyck, Rik; Poortmans, Jef; Zeman, Miro; Isabella, Olindo; Manganiello, Patrizio

DOI
10.1016/j.solmat.2023.112486

Publication date
2023

Document Version
Final published version

Published in
Solar Energy Materials and Solar Cells

Citation (APA)
van Nijen, D. A., Muttillo, M., Van Dyck, R., Poortmans, J., Zeman, M., Isabella, O., & Manganiello, P. (2023). Revealing capacitive and inductive effects in modern industrial c-Si photovoltaic cells through impedance spectroscopy. *Solar Energy Materials and Solar Cells*, *260*, Article 112486. https://doi.org/10.1016/j.solmat.2023.112486

Solar Energy Materials & Solar Cells 260 (2023) 112486

Contents lists available at ScienceDirect

Solar Energy Materials and Solar Cells

journal homepage: www.elsevier.com/locate/solmat

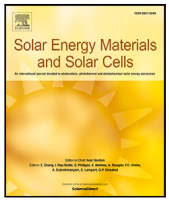

Revealing capacitive and inductive effects in modern industrial c-Si photovoltaic cells through impedance spectroscopy

David A. van Nijen [a,*], Mirco Muttillo [a], Rik Van Dyck [b,c], Jef Poortmans [b,c,d], Miro Zeman [a], Olindo Isabella [a], Patrizio Manganiello [a]

[a] Delft University of Technology, Mekelweg 4, Delft, 2628 CD, The Netherlands
[b] KU Leuven, Oude Markt 13, Leuven, 3000, Belgium
[c] imec, imo–imomec, EnergyVille Campus, Thor Park 8320, Genk, 3600, Belgium
[d] Hasselt University, imo–imomec, Martelarenlaan 42, Hasselt, 3500, Belgium

ARTICLE INFO

Dataset link: https://doi.org/10.4121/0c9538d5-5930-4ae5-a3c7-0a8dbe4b94f5

Keywords:
Photovoltaics
Photovoltatronics
Crystalline silicon
Impedance spectroscopy
Capacitance
Inductance
Partial shading
Shading tolerance

ABSTRACT

To achieve a high performance in sub-module power conditioning circuits, it is important that power converters are designed in accordance with the photovoltaic (PV) cell impedance at the input. Taking this one step further, exploiting the impedance of cell strings could even support novel power conditioning approaches in PV modules. In this work, we characterize the impedance of eight single-cell laminates based on different industrial c-Si PV cell architectures. This characterization is carried out by impedance spectroscopy in dark conditions at room temperature, and the capacitive and inductive effects are evaluated through equivalent model fitting. By comparing the results for the different laminates, it is revealed how the cell design affects its impedance. Our experiments show that the PN junction capacitance at maximum power point varies for the different cells between 0.30 and 45.6 μF/cm^2. The two main factors contributing to a high PV cell capacitance at maximum power point are (i) a low wafer dopant concentration and (ii) a high maximum power point voltage. In high-efficiency c-Si PV cells that will be fabricated in the coming years, increasing capacitances are expected for operation near the maximum power point. Furthermore, the single-cell laminates exhibit inductances between 63 and 130 nH, and our results indicate that the inductance is mostly affected by the number of busbars and the geometry of the metal contacts.

1. Introduction

Photovoltaic (PV) modules based on crystalline silicon (c-Si) cell technology dominate the market [1]. The PV industry mainly produces c-Si-based modules with standardized designs, aimed at producing electricity at low cost under uniform irradiation [2]. However, this conventional design is not optimal in locations where partial shading occurs frequently, such as in urban environments. In these places, the energy yield can be increased up to 25%–30% by making use of so-called shade tolerant PV modules [3,4]. One of the methods to increase the shade tolerance of a PV module is to implement maximum power point tracking (MPPT) at sub-module level [5–7]. This approach allows the operating point of groups of solar cells to be adapted without affecting the operation of the other cells in the PV module. To achieve a high performance in such power conditioning circuits, it is important that the converter is designed in accordance with the solar cell impedance at the input [8]. Taking this one step further, exploiting the impedance of PV cell strings could even support novel power conditioning approaches in PV modules. For example, it has been demonstrated that using self-capacitance for power balancing among different cells can potentially become cost effective [9]. Furthermore, in different types of power converters, an input capacitor is used to reduce the ripple voltage at the input of the converter [10]. If such a converter were used in a PV module to implement MPPT at cell or sub-module level, the self-capacitance of the solar cells could potentially fulfill the function of this input capacitor [11]. Since the capacitor is typically one of the least reliable components in power converters [12], this approach can increase reliability. It was even proposed to extend this concept to low power applications by also exploiting the inductive effects in a PV cell string [13].

To assess the feasibility of the above-mentioned applications, a detailed understanding of the impedance in modern industrial c-Si solar cells is crucial. Impedance spectroscopy is an established method for characterizing the impedance of nonlinear electronic devices such as solar cells [14]. Various impedance spectroscopy studies on c-Si PV

* Corresponding author.
E-mail address: d.a.vannijen@tudelft.nl (D.A. van Nijen).

https://doi.org/10.1016/j.solmat.2023.112486
Received 26 April 2023; Received in revised form 20 July 2023; Accepted 24 July 2023
Available online 5 August 2023

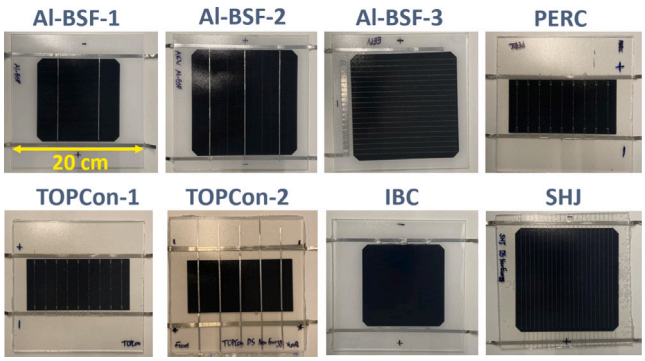

Fig. 1. Photos of the single-cell laminates used for this study. The details of the lamination stacks are presented in Table 1.

cells have already been published, in which dynamic equivalent circuits of the PV cells are typically fitted to the experimental impedance data. For example, several studies have been performed for small-area c-Si PV cells up to 32 cm^2 [8,15–23]. Moreover, there are several reports in the context of fault detection in which impedance spectroscopy is performed on larger cells and modules [24–27]. Furthermore, the authors of [28] have characterized capacitive effects in modern PV modules by performing direct and reverse I–V measurements with a pulsed solar simulator. However, their method does not take into account frequency-dependent effects and is intended to evaluate the minimum pulse time required for an accurate I–V measurement.

In the present manuscript, the impedance of single-cell laminates made with eight different commercial c-Si PV cells are characterized. Among these cells, the main available architectures, such as Aluminium Back Surface Field (Al-BSF), Passivated Emitter and Rear Contact (PERC), Tunnel Oxide Passivated Contact (TOPCon), Interdigitated Back Contact (IBC), and Silicon Heterojunction (SHJ) are included. To the best knowledge of the authors, this is the first work in which the impedance of such a broad range of large-area industrial cells is systematically compared. The measurements are carried out in dark conditions with an in-house designed impedance spectroscopy setup. Furthermore, the capacitive and inductive effects of the cell laminates are evaluated through equivalent model fitting, and the differences are explained by analyzing the underlying physics. This way, it is revealed how the dynamic behavior of a c-Si solar cell is affected by its design.

2. Experimental method

2.1. Cell laminates used for this study

For this study, single-cell laminates were manufactured using eight different industrial c-Si PV cells. The laminates are shown in Fig. 1, and the exact corresponding laminated stacks are presented in Table 1. It is worth noting that the different cells varied in size, as well as in metallization patterns.

For all of the laminates in Fig. 1, I-V measurements were carried out in Standard Test Conditions (STC) as well as dark conditions, which are presented in Fig. 2 and Fig. 3, respectively. These I-V scans were performed using a LOANA solar cell analysis system [29]. The corresponding STC parameters are presented in Table 2, where the global series resistance is found from comparing the J_{sc}–V_{oc} measurement with light-IV and the double light method [29].

2.2. Impedance spectroscopy setup

Commercial impedance spectroscopy setups are typically not suitable to characterize the laminates used in this study. For the large-area cells, DC currents higher than 0.5 A are already exceeded in dark

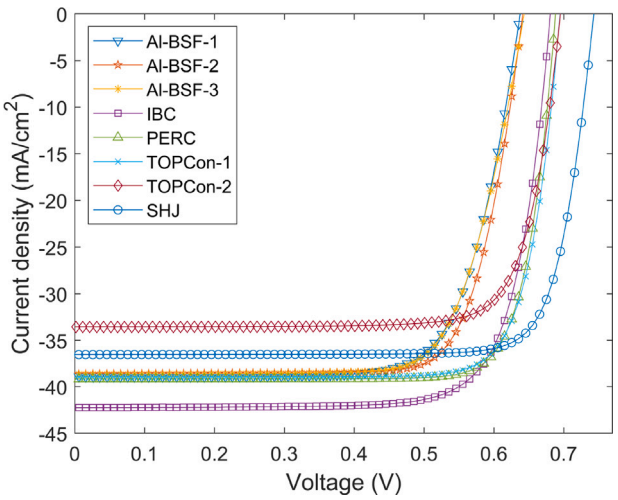

Fig. 2. I-V curves of the single-cell laminates in STC conditions, as characterized using a LOANA solar cell analysis system.

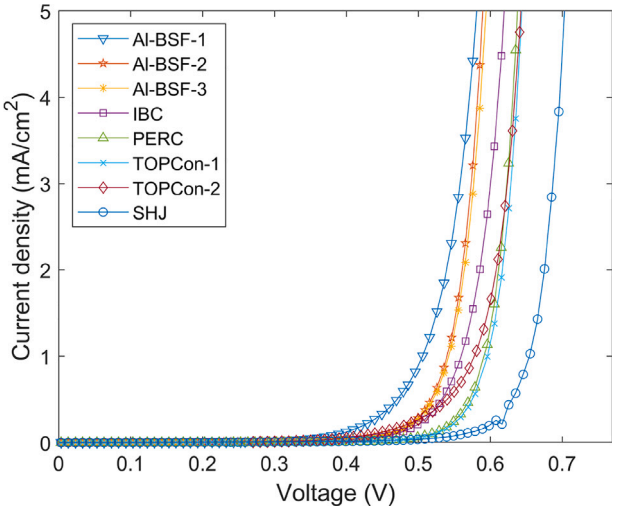

Fig. 3. I-V curves of the single-cell laminates in dark conditions, as characterized with a LOANA solar cell analysis system.

conditions at DC bias voltages around 0.6 V. The characterization of devices at such high DC current and relatively low DC voltage levels using commercial setups is incompatible with the frequency range of interest, which extends into the kHz range (>5 kHz). To characterize the cells in a wide voltage range, an in-house impedance spectroscopy setup was designed, which is schematically represented in Fig. 4. The DC bias and the small-signal sinusoidal waveforms are set through an Agilent 33250 A function generator. The DC voltage on the PV cell is measured using a Keithley 2000 Multimeter. To increase the output current capability of the function generator, an OPA549 op-amp supplied by two EA-OS 2042-20 B power supplies is used in power buffer configuration. For accurate and high-speed analysis of these signals, the impedance data reported in this manuscript are obtained by analyzing the waveforms through lock-in amplifiers. The sinusoidal current signal $\hat{\imath}$ is measured using a Yokogawa 702916 current probe that is connected to a Signal Recovery 7225 DSP lock-in amplifier. The sinusoidal voltage signal $\hat{v}$ is recorded through an EG&G Instruments 7260 DSP lock-in amplifier, where the voltage probe of channel A is connected to the positive contact of the solar cell, and the voltage probe of channel B to the negative side. By using the A-B setting of the lock-in amplifier, the difference between the two input voltages is measured.

Table 1
This table elaborates on the materials and metallization structure that were used for the different laminates. Each row corresponds to one of the laminates in Fig. 1. The term busbar is abbreviated by BB, SmartWire by SW, back-contacted by BC, and a white backsheet from Icosolar PPF by WBS. The SW connection uses round wires with a 200 μm core and a eutectic SnBu solder coating. The glass plates that are used are low Fe borosilicate glass without anti-reflection coating and the encapsulants are commercially available EVA and TPO. The ribbons that are used to connect the cells to external setups are commercial 0.2 mm × 0.5 cm Cu PV ribbons with a eutectic SnBi solder coating.

Laminate ID	Mono (M)/ Bifacial (B)	Cell area (cm^2)	Front	Front encapsulant	Metal front side	Active layer	Metal back side	Rear encapsulant	Back
Al-BSF-1	M	153	glass	EVA	2BB	Al-BSF	2BB	EVA	WBS
Al-BSF-2	M	244.3	glass	EVA	3BB	Al-BSF	3BB	EVA	WBS
Al-BSF-3	M	244.3	glass	EVA	SW, 19 W	Al-BSF	4BB	EVA	WBS
PERC	B	126	glass	TPO	9BB	PERC	9BB	TPO	glass
TOPCon-1	B	126	glass	TPO	9BB	TOPCon	9BB	TPO	glass
TOPCon-2	B	126	glass	TPO	5BB	TOPCon	5BB	TPO	glass
IBC	M	153	glass	EVA	–	IBC	BC	EVA	WBS
SHJ	B	244.3	glass	TPO	SW, 22 W	SHJ	SW, 22 W	TPO	glass

Table 2
STC parameters of the single-cell laminates used for this study, as characterized with a LOANA solar cell analysis system.

Laminate ID	J_{sc} (mA/cm^2)	V_{oc} (mV)	*FF* (%)	η (%)	V_{mpp} (mV)	I_{mpp} (A)	R_s (Ω cm^2)
Al-BSF-1	38.92	637.6	73.44	18.22	506.2	5.51	1.35
Al-BSF-2	38.66	641.3	76.71	19.02	521.4	8.91	1.10
Al-BSF-3	38.65	643.2	73.75	18.33	505.8	8.86	1.65
PERC	39.18	688.1	81.35	21.93	586.6	4.71	0.55
TOPCon-1	38.96	694.7	80.30	21.73	588.6	4.65	0.72
TOPCon-2	33.54	695.1	79.34	18.50	587.4	3.97	0.65
IBC	42.25	680.7	76.97	22.14	566.1	5.98	0.85
SHJ	36.52	743.0	81.52	22.12	635.8	8.50	0.94

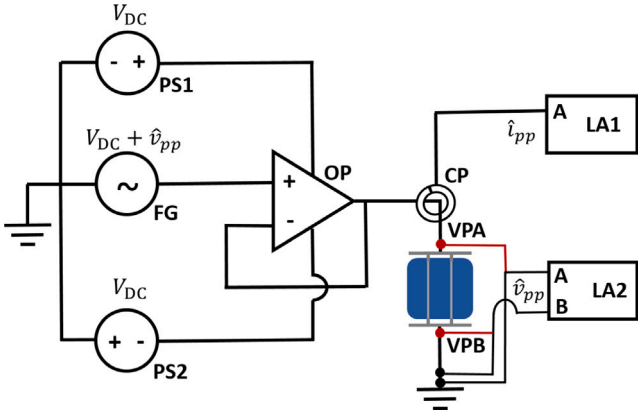

Fig. 4. Overview of the in-house designed impedance spectroscopy setup used for this study. Power supplies 1 (PS1) and 2 (PS2) are both of the type EA-OS 2042-20 B. The function generator (FG) is an Agilent 33250 A, whereas the op-amp (OP) is of the type OPA-549 and is connected in power buffer configuration. Lock-in amplifier 1 (LA1) and 2 (LA2), are a Signal Recovery 7225 DSP and a EG&G Instruments 7260 DSP, respectively. The current probe (CP) is a Yokogawa 702916, and is connected to channel A of LA1. Voltage probe VPA, which is connected to the positive contact of the PV cell, is analyzed through channel A of LA2. Voltage probe VPB, which is connected to the negative side of the PV cell, is analyzed through channel B of LA2.

Since the voltage and current signals are measured separately, parasitic cable influences are limited in a way that is similar to four-terminal sensing. For both lock-in amplifiers the reference channel is connected to the function generator, making it possible for both $\hat{v}$ and $\hat{\imath}$ to extract the rms amplitude and the phase shift relative to the function generator waveform.

The impedance of the PV cells is characterized in a frequency range between 5 Hz and 120 kHz. This upper bound is limited by the maximum frequency of the 7260 DSP lock-in amplifier. Setting the DC bias voltage on the PV cell, performing frequency sweeps with the function generator, and recording the values from the lock-in amplifier were done through an in-house developed Labview program. This level of automation ensures repeatability of the experiments and minimizes human error.

Since solar cells are nonlinear devices, the amplitude of the sinusoidal signal $\hat{v}_{pp}$ that is applied about a DC operating point should be sufficiently small to maintain the linearity of the response [15,16]. In previous work, $\hat{v}_{pp}$ values between 10 mV_{pp} and 28 mV_{pp} are typically chosen for impedance spectroscopy measurements on c-Si PV cells to avoid nonlinearities [8,15–20]. It is worth noting that nonlinearities are most likely to affect measurements in DC bias points where the *I-V* curve exhibits the most curvature. For example, to evaluate the effect of nonlinearities on the impedance measurements performed with the setup in this work, the IBC cell is characterized at V_{DC} = 550 mV with a varying amplitude $\hat{v}_{pp}$. It can be seen in Fig. 3 that this operating point corresponds to a relatively strong curvature in the dark *I-V* curve. In Fig. 5, the impedance data are presented for a frequency range between 25 Hz and 5 kHz in the form of Nyquist impedance spectra. In such a representation, the real part of the impedance is shown on the horizontal axis and its imaginary part on the vertical axis, both in Ohm (Ω). It can be seen how a too high amplitude $\hat{v}_{pp}$ indeed affects the recorded impedance data. Specifically, nonlinearities at higher amplitudes lead to an underestimation of the impedance, and such underestimation becomes smaller with increasing frequency. However, for both $\hat{v}$ and $\hat{\imath}$, a minimum amplitude is required to maintain a good signal-to-noise ratio during a measurement. Especially around zero bias on a PV cell with a high shunt resistance, the current signal is limiting in this respect. In this work, the amplitude is varied depending on the DC bias voltage, where $\hat{v}_{pp}$ is always kept below 3 mV_{pp} around the knee voltage of the dark *I-V* curve.

3. Theory

3.1. PN junction impedance

The diode current that flows across a PN junction is based on the diffusion of charge carriers across the depletion region. By applying the abrupt junction approximation, which assumes that there is an abrupt discontinuity in space charge density between the space charge region and the neutral semiconductor region, an analytic expression can be derived for the current–voltage characteristic of a PN junction [30]:

$$I_d = A\left[\frac{qn_i^2}{N_a}\sqrt{\frac{D_n}{\tau_{n0}}} + \frac{qn_i^2}{N_d}\sqrt{\frac{D_p}{\tau_{p0}}}\right]\left[\exp\left(\frac{qV_F}{nkT}\right) - 1\right] \quad (1)$$

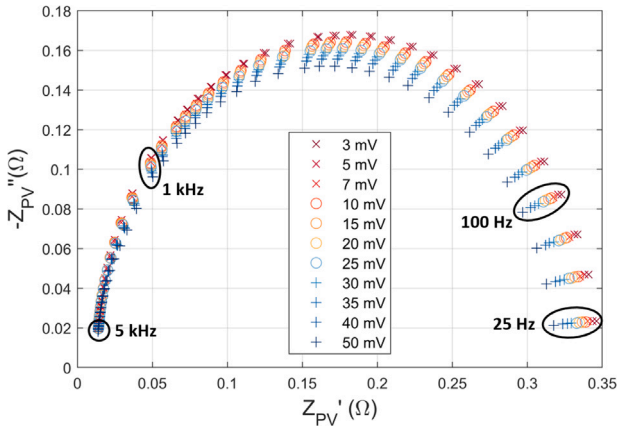

Fig. 5. Experimentally recorded Nyquist spectra for the IBC cell at a DC bias voltage of V_{DC} = 550 mV. The spectra were characterized at a varying peak-to-peak amplitude $\hat{v}_{pp}$ of the small sinusoidal signal, as indicated in the legend.

where A is the cross-sectional area of the PN junction, q is the elementary charge constant, n_i is the intrinsic carrier concentration, and N_a and N_d are the acceptor and donor concentrations. D_p and D_n are the diffusion constants of holes and electrons, τ_{p0} and τ_{n0} are the minority charge carrier lifetimes, and V_F is the applied forward-bias voltage. The parameter n is called the ideality factor, and varies from $n \approx 1$ for low forward bias voltage to $n \approx 2$ for large forward bias voltage. Finally, k and T are the Boltzmann constant and temperature, respectively.

Furthermore, as the capacitive behavior of c-Si solar cells originates in their junctions, it is worth reviewing the two main capacitive components of which any PN junction is constituted. The depletion capacitance is the capacitance that is associated with the ionized donor and acceptor atoms in a depletion region of a PN junction. It is influenced by the dopant concentrations and the applied voltage, since these factors affect the depletion region width and charge density. The depletion capacitance can be expressed by the following equation if the abrupt junction approximation is applied [30]:

$$C_{dep} = A\sqrt{\frac{q\epsilon_s N_a N_d}{2\left(V_{bi} + V_R\right)\left(N_a + N_d\right)}} \tag{2}$$

where ϵ_s is the permittivity of the semiconductor, V_{bi} the built-in potential, and V_R is the applied reverse-bias voltage.

The diffusion capacitance is the capacitance that is associated with the build-up of minority carrier charge in the quasi-neutral regions. The diffusion current has an exponential dependence on the applied forward bias voltage. The diffusion capacitance can be expressed by the following equation if the abrupt junction approximation is applied [30]:

$$C_{dif} = \frac{q^2 n_i^2 A}{2kT}\left(\frac{\sqrt{D_p \tau_{p0}}}{N_d} + \frac{\sqrt{D_n \tau_{n0}}}{N_a}\right)\exp\left(\frac{qV_F}{kT}\right) \tag{3}$$

It is worth noting that this expression for the diffusion capacitance only holds when the assumptions $\omega\tau_{p0} \ll 1$ and $\omega\tau_{n0} \ll 1$ are valid [30], where ω is the radian frequency of the small signal. Above this characteristic frequency, the minority carrier excess densities are no longer able to follow the AC signal and the C_{dif} contribution to the total capacitance relaxes [31].

As can be deduced from Eqs. (2) and (3), the total capacitance exhibited by PN junctions is dominated by the depletion capacitance at low applied forward bias voltages. At higher voltages, the total capacitance becomes dominated by the exponentially increasing diffusion capacitance, although also the depletion capacitance increases because of the term $V_{bi} + V_R$ in the denominator.

3.2. Dynamic equivalent solar cell model

There are typically two junctions present in c-Si solar cells, which are the PN junction and the low-high (LH) junction. Notably, modern solar cells are increasingly adopting passivating contacts [32]. For instance, in SHJ structures the band bending is induced by doped amorphous Si layers [33,34]. Moreover, there have even been demonstrations of dopant-free selective contacts with a MoO_x hole collector [35]. Considering the rise of passivating contacts, it is important to mention that both passivating and non-passivating carrier selective contacts typically obey the same current–voltage characteristic from Eq. (1). This holds true for passivating contacts only when they are highly selective, resulting in minimal voltage losses in the contact region. In solar cells these conditions are usually achieved due to their carrier selective contacts with appropriate work functions and high-quality surface passivation [36]. On the contrary, Eq. (1) does not directly apply to LH junctions. The LH junction establishes a built-in potential that repels minority carriers from the contacts that collect majority carriers. However, since the minority carriers do not switch into majority carrier after crossing the LH junction, the space charge region does not develop into a depletion region. Thus, an important difference between PN junctions and LH junctions is that the LH junction does not exhibit a high diffusion resistance in reverse bias [37], whereas the PN junction around zero bias voltage does show such a high diffusion resistance that the practical resistance of the PN junction becomes limited by the shunt resistance [38]. Additionally, the absence of a depletion region in the LH junction implies that its capacitance only shows the behavior of a diffusion capacitance, and not that of a depletion capacitance [20].

Using the concepts described above, a dynamic equivalent solar cell model can be defined. In this work, the equivalent circuit in Fig. 6(a) is used to fit the experimental impedance data recorded for the different laminates. The circuit contains two parallel RC-circuits, a series resistance R_s, and an inductor L_s. The R_j–C_j loop corresponds to the PN junction, and the R_{LH}–C_{LH} loop to the LH junction of the PV cell. To relate the components in Fig. 6(a) to the physics in the PV cell, Fig. 6(b) is included. When comparing these circuits, it can be observed that R_j denotes the parallel of the diode resistance R_d and the shunt resistance R_{sh}. Moreover, C_j represents the net capacitance of C_{dep} and C_{dif}. Furthermore, the inductor L_s in Fig. 6 accounts for the inductive reactance in the laminate, which is mostly a result of the current traveling through the interconnection and cell metallization and is most prominent in the high frequency end of the impedance spectrum.

3.3. Equivalent model fitting

The impedance of the circuit in Fig. 6(a) is described by the following equation:

$$Z_{PV} = j\omega L_s + R_s + \left[R_j \parallel \frac{1}{j\omega C_j}\right] + \left[R_{LH} \parallel \frac{1}{j\omega C_{LH}}\right] \tag{4}$$

where j denotes the imaginary unit, R_j is the PN junction resistance, and C_j is the PN junction capacitance. Eq. (4) can be rewritten into the form $Z_{PV} = Z'_{PV} + jZ''_{PV}$ with the resistance Z'_{PV} and the reactance Z''_{PV} being defined as follows:

$$Z'_{PV} = R_s + \frac{R_j}{1 + R_j^2\omega^2 C_j^2} + \frac{R_{LH}}{1 + R_{LH}^2\omega^2 C_{LH}^2} \tag{5}$$

$$Z''_{PV} = \omega L_s - \frac{R_j^2\omega C_j}{1 + R_j^2\omega^2 C_j^2} - \frac{R_{LH}^2\omega C_{LH}}{1 + R_{LH}^2\omega^2 C_{LH}^2} \tag{6}$$

In Eq. (6), the occurrence of negative or positive signs can be attributed to the distinct behavior of current and voltage in capacitors and inductors. Specifically, in a capacitor, the current leads the voltage, resulting in a negative sign, whereas in an inductor, the current lags behind the voltage, leading to a positive sign. To determine the values

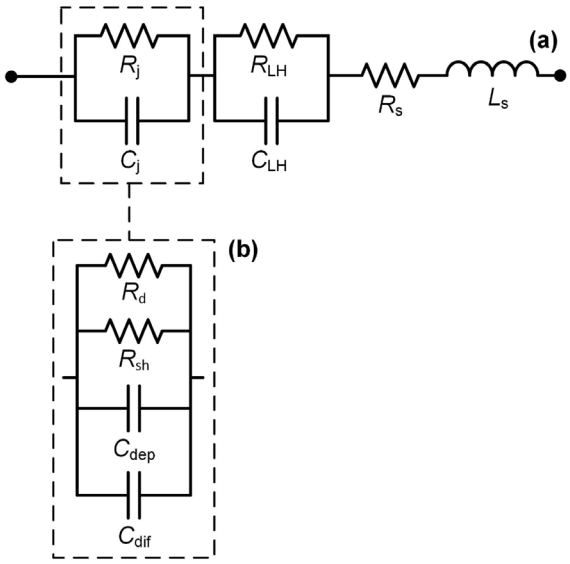

Fig. 6. (a) Electrical equivalent model used in this study to fit the experimentally recorded impedance data of the single-cell laminates. The R_j–C_j and R_{LH}–C_{LH} loops represent the impedance of the junctions in the PV cell. R_s and L_s denote the series resistance and inductance, respectively. (b) A more detailed equivalent circuit that clarifies how the R_j–C_j loop corresponds to the cell physics. It is shown that R_j represents the parallel of the diode resistance R_d and shunt resistance R_{sh}, whereas C_j is constituted of the parallel of C_{dep} and C_{dif}.

of the circuit parameters in Fig. 6(a) at any DC operating voltage V_{DC}, Eqs. (5) and (6) are simultaneously fitted to the recorded impedance data through complex nonlinear least-squares (CNLS) analysis [39]. For the fitting procedure, the MATLAB *lsqcurvefit* solver is used, with the fitting parameters being C_j, R_j, C_{LH}, R_{LH}, L_s, and R_s. It is worth noting that at low V_{DC} values, the Nyquist spectra of the different laminates closely resemble semi-circles, which implies that the R_j–C_j loop dominates the total PV impedance. At higher bias voltages, the Nyquist spectra deviate from the semi-circular shape due to the combined influence of the other components from Fig. 6(a). For the CNLS analysis in this work, a PV model consisting of only the R_j–C_j loop is used at low V_{DC} values, whereas the full model from Fig. 6(a) is used at higher V_{DC} values. To determine from which V_{DC} value it becomes necessary to use the full impedance model, it is checked whether the fitting quality with only the R_j–C_j loop exceeds certain error thresholds. In this work the error metrics Root Mean Square Error (RMSE) and Normalized Root Mean Square Error (NRMSE) are used, which are further explained in Appendix A. Furthermore, a detailed description of the fitting procedure is presented in Appendix B.

4. Results and discussion

The impedance of each cell laminate was characterized from short-circuit to well above V_{mpp} in steps of maximum 0.1 V. In Fig. 7, the experimentally recorded impedance data for the IBC laminate, as well as the CNLS fits to the data are presented. This same procedure was followed for the other seven laminates, and the resulting values for all the circuit elements in the PV dynamic model are presented for varying V_{DC} in Appendix C. In the remainder of this section, the most important findings are summarized. The focus is on the best-fit values for the R_j–C_j loop and L_s of the dynamic equivalent circuit in Fig. 6(a). Since these circuit elements constitute the main fraction of the total PV impedance, they are the most physically relevant and can be fitted with the highest accuracy.

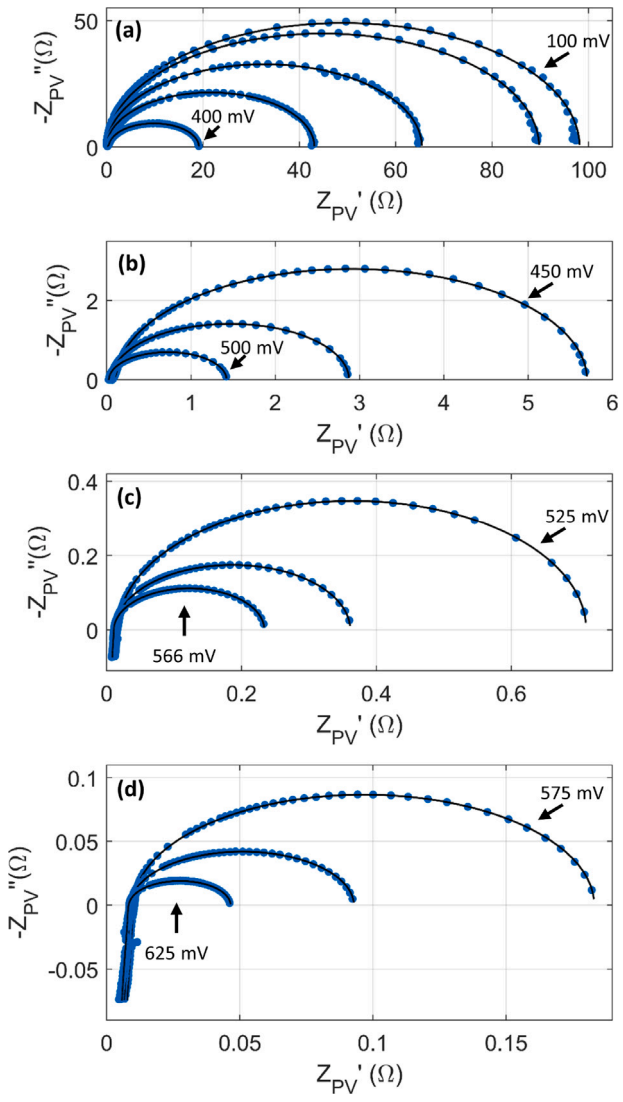

Fig. 7. Nyquist spectra for the IBC cell recorded at various DC voltages. The symbols represent experimental data and the lines are CNLS fits to the data using the circuit model of Fig. 6(a). In 7(a), the plots of successively decreasing radii were collected at gradually increasing applied DC bias voltages in the following order: V_{DC} = 100, 200, 300, 350, and 400 mV. In 7(b), the plots of large to small radii correspond to 450, 475, and 500 mV. The plots of successively decreasing radii in 7(c) were recorded at 525, 550, and 566 mV (V_{mpp}). In 7(d), the plots of large to small radii correspond to 575, 600, and 625 mV.

4.1. PN junction capacitance

Since the R_j–C_j loop dominates the total impedance of the different cells that were tested, C_j has a strong impact on the total impedance. The areal PN junction capacitance C_j^A, which is C_j normalized to the PV cell area, is presented in Fig. 8 as a function of the applied V_{DC}. As expected from Eq. (3), an exponentially increasing capacitance as a function of applied V_{DC} is observed in the high forward-bias region. The slight deviations from this exponential trend can most likely be explained by the fact that the effective voltage over the R_j–C_j loop is slightly lower than the applied voltage [20]. Indeed, a small fraction of the applied voltage drops over R_s, and this fraction increases for increasing V_{DC}.

It is shown in Eq. (3) that the minority carrier lifetime τ_{min} is one of the parameters affecting the diffusion capacitance. Indeed, a high τ_{min} is typically mentioned in literature as an important reason for high diffusion capacitances in high-efficiency cells [28]. To cross-check this

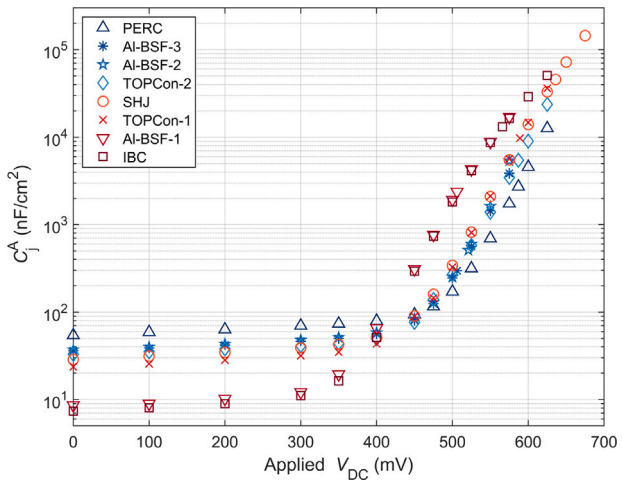

Fig. 8. The areal C_j^A of the cell laminates as a function of applied DC bias voltage, which is obtained by fitting the circuit in Fig. 6(a) to the experimentally recorded impedance data through CNLS analysis.

with our results in Fig. 8, it is important to realize that a change in τ_{min} does not affect the slope of the capacitance–voltage (C_j^A–V) curve, but only shifts the curve horizontally in the high forward-bias region. Taking into account that the V_{oc} is a good indicator of the minority carrier lifetime [40], it could be expected that the curves shifted the most to the left correspond to the cells with the highest V_{oc}. However, when comparing the results in Fig. 8 to the V_{oc} values in Table 2, no such trend is observed. On the contrary, for the cell with the lowest V_{oc} (Al-BSF 1), the C_j^A–V curve in the high forward bias region is among the two cells for which the curve is shifted the furthest to the left. These results suggest that τ_{min} is not the most important factor affecting the shape of the C_j^A–V curve of c-Si solar cells.

For interpreting Fig. 8, a more useful starting point is the low-voltage region, where C_j^A is dominated by the depletion capacitance $C^A_{j,dep}$. As described in Eq. (2), the depletion capacitance is governed by the dopant concentrations around the PN junction. To further analyze C_j^A in the low-voltage region, it is worth noting that c-Si PV cells typically exhibit two characteristics that facilitate a simplified analysis. Firstly, the depletion region of the PN junction usually extends into the bulk of the wafer. Indeed, in simulated band diagrams of PV cells based on TOPCon [41] and SHJ technology [42,43], it is shown that the band bending extends into the bulk of the wafer. Secondly, the substrate doping density N_{sub} – also known as wafer dopant concentration – is typically much lower than that of the charge-carrier selective layer on the other side of the PN junction. When these two conditions are satisfied, the PN junction can be treated like a one-sided junction, which is defined as a PN junction where one side is much more heavily doped than the adjacent side [30]. In that case, the expression for the depletion capacitance from Eq. (2) simplifies to:

$$C_{dep} = A\sqrt{\frac{q\epsilon_s N_{sub}}{2\left(V_{bi}+V_R\right)}} \tag{7}$$

which implies that the depletion capacitance in a c-Si PV cell is primarily determined by N_{sub} and V_{bi}. In fact, both these parameters can be extracted from the $1/C^2$ versus V_{DC} relationship in the bias voltage region where $C_{j,dep}$ is dominant. Specifically, N_{sub} can be obtained from the slope of this curve, while V_{bi} can be determined from the voltage at which a linear fit to the $1/C^2$ data crosses zero [30,44]. To extract these values from the different laminates, capacitance–voltage (C-V) measurements are conducted at 10 kHz between V_R = 2.0 V and V_F = 0.3 V. The resulting N_{sub} and V_{bi} values are presented in Table 3.

It appears that among the different laminates, N_{sub} exhibits a much wider spread than V_{bi}. Whereas N_{sub} can vary by as much as a factor

Table 3
Substrate dopant density N_{sub} and built-in potential V_{bi} of all laminates as extracted from C-V measurements at 10 kHz between V_R = 2.0 V and V_F = 0.3 V. The measurements were carried out using an HP 4284A precision LCR meter.

Laminate ID	N_{sub} (atoms × cm^{-3})	V_{bi} (V)
Al-BSF-1	4.2×10^{14}	0.57
Al-BSF-2	1.1×10^{16}	0.63
Al-BSF-3	1.0×10^{16}	0.64
PERC	2.6×10^{16}	0.74
TOPCon-1	4.5×10^{15}	0.65
TOPCon-2	1.0×10^{16}	0.77
IBC[a]	4.5×10^{14}	0.64
SHJ	5.6×10^{15}	0.56

[a]Only C-V data between V_R = 0.5 V and V_F = 0.3 V was used. In the case of an IBC structure, a too high reverse bias voltage may lead to interaction between neighboring fingers.

62, the V_{bi} variation is limited to a factor 1.4. Therefore, it can be concluded that the depletion capacitance in a c-Si PV cell is mainly determined by N_{sub}. In Fig. 8, the marker color transition from blue to red (transition from △ to □) visualizes a decreasing areal depletion capacitance $C^A_{j,dep}$.

Furthermore, upon closer examination of Fig. 8, a consistent trend can be observed: the lower C_j^A is in the low-voltage region, the more the curve is shifted to the left in the high-voltage region. This trend suggests that N_{sub} does not only govern the depletion capacitance in the low-voltage region, but also the diffusion capacitance in the high-voltage region. Indeed, Eq. (3) shows that the diffusion capacitance is directly dependent on the dopant concentrations outside the depletion region. The results in this work show that the substrate doping density affects the shape of the C_j^A–V curve of a c-Si PV cell much more than the minority carrier lifetime.

Since a low N_{sub} shifts the C_j^A–V relationship in the high-voltage region to the left in Fig. 8, a low N_{sub} contributes to reaching a high diffusion capacitance at V_{mpp}. However, when comparing the capacitance of the different cells, it is important to realize that in practice they will operate at different voltages due to their different V_{mpp} values. The lowest and highest C_j^A values in this work for an applied voltage equal to the V_{mpp} in STC conditions, are 0.30 μF/cm^2 for the Al-BSF-3 cell and 45.6 μF/cm^2 for the SHJ cell. It is worth pointing out that in Fig. 8 the C_j^A–V curve of the SHJ cell is shifted to the right compared to the IBC cell in the high voltage region. Nevertheless, the reason that the SHJ cell still has the highest C_j^A value for operation around maximum power point is its high V_{mpp} of 636 mV in STC conditions.

4.2. Outlook for capacitive effects in PV cells

Since the results in this work show that the capacitive effects in solar cells are mostly governed by the substrate doping density, it is worth to discuss how N_{sub} affects the performance of c-Si PV cells, and to analyze the latest trends in industry.

Traditionally, in Al-BSF cells, recombination at the full-area metal rear contact limits the total minority charge carrier lifetime τ_{min} [33]. Even for industrial n-type TOPCon cells with efficiencies over 23%, it has been reported that recombination at the front and back sides is still limiting τ_{min} [45]. As long as recombination in the bulk of the wafer is not limiting τ_{min}, the bulk carrier lifetime τ_{bulk} does not have a strong impact on the V_{oc}. On the one hand, to ensure that τ_{bulk} is indeed sufficiently high and does not limit τ_{min} in practice, in the past manufacturers used wafers with a relatively high N_{sub} [45]. Substrates with an increased N_{sub} have a higher tolerance to Shockley–Read–Hall (SRH) defects [46,47]. On the other hand, using wafers with a lower N_{sub} can increase the short-circuit current I_{sc}. It is worth noting that it varies for the different c-Si cell technologies how strongly I_{sc} is affected by N_{sub}, and which physical processes govern this effect [33,45,46]. Furthermore, it is worth noting that N_{sub} has an impact on *FF*, which

varies for different PV cell technologies and geometries [33]. In practice, the optimum N_{sub} in industrial c-Si PV cells can be considered a trade-off between maximizing I_{sc} while ensuring a sufficiently high τ_{bulk} for wafers produced in mass quantities [45,46]. Nowadays, the optimum is shifting to lower N_{sub} values. Recent improvements in the Czochralski (Cz) process have ensured that the major share of the PV wafer market is now based on monocrystalline ingots grown via the Cz method [48]. As the quality of the wafers is improving, it becomes technologically possible to manufacture high-quality silicon wafers with a lower N_{sub} [45].

Furthermore, due to the progress in surface passivation technology and wafer pretreatment [49,50], we are nearing the point where recombination in the bulk starts to limit τ_{min} in industrial c-Si PV cells. For the Cz wafers that are nowadays used in industrial PV cells, τ_{bulk} is usually still limited by SRH recombination [46]. Nevertheless, for SHJ PV cell precursors based on n-type Cz wafers, implied V_{oc} values have already been achieved that are only 9 mV away from the intrinsic limit [51]. Furthermore, these previously predicted intrinsic limits are even being exceeded by recent reports on monocrystalline silicon float zone wafers passivated with TOPCon contact stacks [49,52]. If the τ_{bulk} in modern wafers indeed becomes limited by Auger recombination, it becomes relevant to mention that the efficiency limit for c-Si PV cells is the highest for a wafer bulk made of undoped silicon [53,54]. This is related to the fact that the intrinsic Auger recombination rate R_{intr} in the bulk of the wafer reduces for a lower N_{sub} [55,56], leading to a higher limit for the V_{oc}. It is worth noting that R_{intr} particularly increases for an N_{sub} above $\sim 10^{15}$ cm^{-3} for n-type Si and above $\sim 10^{16}$ cm^{-3} for p-type Si [53].

Concluding, in high-efficiency c-Si PV cells, increased use of wafers with a low substrate doping density is likely to happen in the future. Furthermore, these cells will likely operate at higher V_{mpp} values. As such, the authors expect the MPP capacitance of industrial c-Si PV cells to increase over the coming years. It is important to note that the cell capacitance exhibits a linear dependency on the solar cell area. Additionally, the equivalent capacitance of a string of cells varies inversely with the number of series-connected cells in that particular string. Consequently, the prevailing industry trends concerning wafer size and the number of cells within a module will directly influence the capacitance observed at module-level.

4.3. Inductive effects

Research has been emerging on exploiting inductive effects in PV cell strings [11,13], and to the best of the authors' knowledge, there have been no previous reports on inductive effects in full-sized industrial cells. The inductance values of the cell laminates that are reported in Appendix C suggest that the inductance is independent of V_{DC}. This is within expectation, since most of the inductive effects presumably originate in the wiring and metal interconnections of the PV cells. Since the inductive reactance makes up a larger share of the impedance at higher V_{DC}, the CNLS fitted values at the highest bias voltages give the best indication of the inductance of the laminate. Thus, the inductances obtained by fitting the impedance data at the seven highest bias points for each laminate are used for a statistical analysis, which is presented in Fig. 9. The corresponding details concerning the cell metallization and wirings in the laminates are presented in Table 1.

Regarding the interpretation of the inductances in Fig. 9, it is important to take into account that part of the inductance in the laminates does not originate in the PV cells themselves, but rather in the metal ribbons within the laminates. Thus, when it comes to inductance, in this manuscript the terminology *laminate* is used instead of *cell*. First of all, it is worth noting that the cells in the laminates have different areas, implying different lengths of their metal contacts. It is expected that longer wires result in larger inductances [57]. However, in Fig. 9 it is shown that the 5-inch cell laminates Al-BSF-1 and IBC have higher inductances than those of the 6-inch cells Al-BSF-2 and Al-BSF-3. This

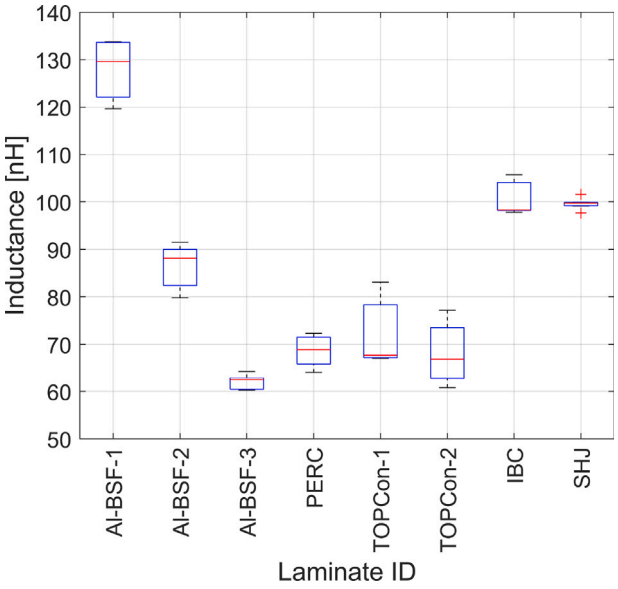

Fig. 9. Statistical analysis regarding the inductance of the cell laminates. The values for the inductance are obtained by fitting the circuit in Fig. 6(a) to the experimentally recorded impedance data through CNLS analysis. The values used to generate this figure correspond to the seven highest DC bias voltages that were recorded for each laminate.

suggests that there are other factors in the cell design that have a larger effect on the resulting inductance. It seems that cell laminates with a similar metallization structure, such as the bifacial 5BB/9BB laminates (PERC, TOPCon 1, TOPCon 2) have a similar inductance between 63–70 nH. When considering all the cells with a busbar metallization, namely Al-BSF-1, Al-BSF-2, PERC, TOPCon-1, and TOPCon-2, it seems that an increase in the number of busbars decreases the inductance. This is in accordance with theory, for which the equivalent inductance scales inversely with the number of inductors connected in parallel. For an increase in the number of busbars from 5 (TOPCon 2) to 9 (PERC, TOPCon 1) the decrease in L_s is marginal, suggesting that most of the inductive effects are originating in the ribbons that are externally connected to the cells.

However, in Fig. 9 it is shown that the IBC and SHJ cell laminates have a relatively high inductance, in spite of their high number of parallel metal lines in the metallization. It is known that for a straight wire both the shape and the cross-sectional area A_{cross} affect the self-inductance, and a smaller A_{cross} typically yields a larger inductance [57]. Thus, the relatively high inductances in the IBC and SHJ laminates could be due to the difference in shape and cross-section of the metal patterns compared to the cells with a more classical busbar metallization. Furthermore, it is worth noting that there is a relatively small space between the metal contacts in the case of the IBC cell, which could cause magnetic interaction between neighboring metal fingers. Finally, it is worth commenting on the Al-BSF-3 laminate, which has SW front metallization. In spite of this, the current collection at the rear of this cell is still happening through 4 busbars. Therefore, the equivalent inductance is a combination of the effect of the many smart wires and the busbars.

4.4. Validity of the impedance model

In general, the CNLS analysis performed in this work yields high-quality fits to the experimental data. Nevertheless, it was observed that the fits become less accurate when the applied DC bias voltage approaches V_{oc}, and these deviations are mostly occurring in the high-frequency region. Several factors could be contributing to these deviations, among which the following three. Firstly, since the impedance of the PV cells is lowest at high frequency and at high V_{DC}

values, measurement errors could become more apparent. Secondly, high-frequency electromagnetic effects such as skin effect could play a role. Thirdly, the conditions $\omega\tau_{p0} \ll 1$ and $\omega\tau_{n0} \ll 1$ may no longer be valid, meaning that the diffusion capacitance is no longer frequency-independent. Nevertheless, since the fits were satisfactory for all cell laminates for DC bias voltages up to V_{mpp}, the authors chose to not further pursue this limitation of the dynamic PV impedance model. For each impedance fit reported in this work, a quantitative assessment of the fitting quality is included in Appendix C.

5. Conclusions

In this work, the impedance of eight single-cell laminates based on different industrial c-Si PV cells was characterized. The capacitive and inductive effects in the laminates were evaluated by fitting a dynamic PV equivalent circuit to the experimentally recorded impedance data through complex nonlinear least-squares analysis.

The experiments show that the PN junction capacitance at maximum power point varies for the different cells between 0.30 and 45.6 μF/cm^2. The two main factors contributing to a high PV cell capacitance at maximum power point are (i) a low wafer dopant concentration and (ii) a high maximum power point voltage. Upon analyzing the trends in upcoming high-efficiency c-Si PV cells, increasing capacitances are expected in the future. Furthermore, the studied cell laminates exhibit inductances between 63 and 130 nH. When comparing the inductive effects between the different laminates, it appears that the inductance decreases when the metallization structure consists of a higher number of busbars. Furthermore, the geometry of the metal contacts affects the inductance.

The findings in this work have some practical consequences. For instance, the minimum time that is required for accurate *I-V* measurements, which is limited by the cell capacitance, must be set accordingly. Nevertheless, the increasing capacitance in modern solar cells will also offer opportunities, as the first publications where the impedance of PV cell strings is exploited have already been emerging.

CRediT authorship contribution statement

David A. van Nijen: Conceptualization, Methodology, Software, Validation, Formal analysis, Investigation, Data curation, Writing – original draft, Writing – review & editing, Visualization, Project administration. **Mirco Muttillo:** Methodology, Software, Validation, Writing – review & editing. **Rik Van Dyck:** Methodology, Writing – review & editing. **Jef Poortmans:** Writing – review & editing. **Miro Zeman:** Funding acquisition. **Olindo Isabella:** Writing – review & editing, Supervision, Funding acquisition. **Patrizio Manganiello:** Conceptualization, Methodology, Software, Formal analysis, Writing – review & editing, Supervision, Project administration.

Declaration of competing interest

The authors declare that they have no known competing financial interests or personal relationships that could have appeared to influence the work reported in this paper.

Data availability

The authors are planning to publish these files in the 4TU ResearchData Archive with the following DOI: https://doi.org/10.4121/0c9538d5-5930-4ae5-a3c7-0a8dbe4b94f5.

Acknowledgments

This work is supported by the sector plan of the Dutch government in photovoltatronics research. Furthermore, the authors thank Stefaan Heirman for his contributions to the experimental setup, and thank Dr. René van Swaaij for the insights he gave during discussions.

Appendix A. Fitting quality assessment

In this work, two metrics are used to quantitatively assess the fitting quality. The first metric is the Root Mean Square Error (RMSE), which is calculated as follows:

$$\mathrm{RMSE} = \sqrt{\frac{\sum_{i=1}^{n} \left(X_{\mathrm{exp}} - X_{\mathrm{model}}\right)^2}{n}} \tag{8}$$

where X_{exp} is the experimentally recorded data, X_{model} is the value that is predicted by the model with the best-fit circuit element values, and n represents the number of data points. Furthermore, to calculate the Normalized Root Mean Square Error (NRMSE), the RMSE is normalized to the range of observed data as follows:

$$\mathrm{NRMSE} = \frac{\mathrm{RMSE}}{X_{\mathrm{exp,max}} - X_{\mathrm{exp,min}}} \tag{9}$$

where $X_{\mathrm{exp,max}}$ and $X_{\mathrm{exp,min}}$ are the highest and lowest value of the experimentally recorded dataset, respectively.

In this work, the NRMSE is used to assess the fitting quality for the magnitude ($\mathrm{NRMSE_M}$), the real part of the impedance ($\mathrm{NRMSE_R}$), and the complex part of the impedance ($\mathrm{NRMSE_X}$). The normalization is done to obtain a fair comparison between impedance measurements at different DC bias voltages. For instance, the magnitude of the impedance is significantly higher at low bias voltages than at high bias voltages. Whereas the magnitude, resistance and reactance are represented on linear scales, the phase is represented on a periodic scale (which repeats after a certain value). Thus, in this work the choice was made to directly use the RMSE_θ without normalization to assess the phase fitting quality for the phase.

Appendix B. Fitting procedure

In this section, the used fitting procedure is explained in detail. In Appendix B.1, some background is given on the challenges involved in the development of a generalized fitting procedure. In Appendix B.2 the fitting approach used in this work is explained. The exact initial values and boundary conditions are described in Appendices B.3 and B.4.

B.1. Challenges in developing a generalized fitting procedure

In general, the R_j–C_j loop in the circuit of Fig. 6 dominates the impedance of the PV cell laminate and can be fitted with high accuracy for all laminates at all DC bias voltages (V_{DC}). However, the main challenge in optimizing the fitting procedure is that it varies with V_{DC} how large a fraction the other circuit elements make up of the total PV impedance. When a circuit element constitutes only a small fraction of a certain impedance measurement, the true value of this component cannot always be extracted. In such cases it is possible that the CNLS solver finds good fits, but not with element values that are physically correct. For instance, the impedance fraction of L_s is relatively small at low V_{DC} values. This can result in an optimum fit where the solver shorts the inductor from the circuit. However, at higher V_{DC} the impedance fraction of L_s increases, and the best-fit circuit values converge towards physically realistic numbers. Thus, for the analysis of L_s, the fits at high DC bias voltages are the most reliable.

Furthermore, in previous work it was reported that the R_{LH}–C_{LH} loop typically remains undetected at low DC bias voltages [20]. In this region, the R_j–C_j loop dominates the PV impedance, which implies that the Nyquist spectrum closely resembles a semicircle. For V_{DC} values where the impedance of the R_{LH}–C_{LH} loop becomes non-negligible, the spectra deviate from the semi-circular nature [8]. In the present work it was indeed found for all laminates that for some V_{DC} values it is necessary to include the R_{LH}–C_{LH} loop in the PV impedance model, whereas for other V_{DC} values the R_{LH}–C_{LH} loop is not detectable. There are also in-between cases where the R_{LH}–C_{LH} loop has only a

Table 4
Best-fit values for the Al-BSF-1 cell laminate.

V_{DC} (mV)	C_j (μF)	R_j (Ω)	C_{LH} (μF)	R_{LH} (Ω)	R_s (mΩ)	L_s (nH)	$NRMSE_M$ (–)	$RMSE_\theta$ (–)	$NRMSE_R$ (–)	$NRMSE_X$ (–)
0	1.315	1110	–	–	–	–	0.0055	1.888	0.0078	0.0107
100	1.373	445.2	–	–	–	–	0.0041	1.260	0.0051	0.0096
200	1.560	143.8	–	–	–	–	0.0049	1.021	0.0051	0.0108
300	1.853	25.16	–	–	–	–	0.0041	0.928	0.0043	0.0085
350	2.967	9.026	2.052	0.231	4.41	44.3	0.0059	3.330	0.0064	0.0129
400	10.06	3.164	5.258	0.254	17.64	122.5	0.0042	0.779	0.0043	0.0088
450	47.42	1.284	7.107	0.0655	10.39	121.1	0.0040	0.724	0.0041	0.0073
475	117.0	0.792	0.191	0.0268	13.68	119.6	0.0037	1.035	0.0040	0.0049
500	295.1	0.460	0.0389	0.0100	15.12	129.5	0.0041	1.801	0.0062	0.0052
506[a]	366.5	0.397	0.0015	0.0136	13.99	124.7	0.0031	0.720	0.0033	0.0034
525	659.8	0.259	1.750	0.0041	15.01	133.5	0.0061	2.177	0.0097	0.0062
550	1353	0.135	0.108	0.0033	13.58	133.8	0.0115	2.551	0.0182	0.0075
575	2614	0.0630	0.0001	0.0015	14.24	133.4	0.0159	2.938	0.0381	0.0091

[a]Denotes the V_{DC} corresponding to the maximum power point.

subtle influence on the Nyquist spectrum and the CNLS solver cannot distinguish between the impedance of the R_{LH}–C_{LH} loop and R_s. For instance, sometimes it was observed that the R_{LH}–C_{LH} loop gets shorted, and the best-fit circuit element for R_s is increased beyond its 'real' value to compensate this. Indeed, for some impedance spectra the way that the R_{LH}–C_{LH} loop and R_s can compensate each other during the fitting procedure proved to be the main challenge. The standard method to solve this is to apply boundary values to the circuit elements during the CNLS analysis. However, in most of the previous work on PV cell impedance there is no mention of boundary conditions used in the fitting procedure. Moreover, in the present work it proved challenging to find generalized boundary conditions that ensure correct fitting results for all circuit elements for all the eight laminates. Since the cells in this work were based on different cell technologies with presumably different LH junction characteristics [33], it was chosen to avoid applying generalized boundary values to the LH junction. Furthermore, since from previous work it is already known that R_s varies with V_{DC} [58], R_s should not be fixed at a global R_s value for the different V_{DC} values. Nevertheless, to still limit the interchangeability between R_s and the R_{LH}–C_{LH}, in this work an upper and lower limit are applied to R_s. These limits are based on the global R_s value as extracted by the LOANA measurement ($R_{s,LOANA}$). More specifically, the upper and lower boundaries are fixed at $0.5 \times R_{s,LOANA}$ and $2 \times R_{s,LOANA}$. Previous research on the bias voltage-dependency of the series resistance of solar cells showed that this is the typical range in which the series resistance varies [58].

B.2. Fitting approach

Based on the challenges mentioned in the previous Appendix B.1, this section elaborates on the fitting approach used in this work. First of all, it is worth noting that for all eight laminates in this work the R_j–C_j loop dominates the PV impedance at low V_{DC} values. Indeed, for V_{DC} values between 0 and 300 mV, accurate fits are already achieved by using a PV impedance model that contains only the R_j–C_j loop. Thus, for each V_{DC}, fits are performed with (i) only the R_j–C_j loop and (ii) the full PV impedance model from Fig. 6. These fitting approaches are from now on called (i) *PN fitting*, and (ii) *full model fitting*, respectively. The error metrics from Appendix A are used to evaluate which model is the most suitable. This is done as follows:

1. For each *PN fit*, it is evaluated whether $NRMSE_M$, $NRMSE_R$ and $NRMSE_X$ are smaller than 0.015. Furthermore, it is checked if $RMSE_\theta$ is smaller than 2.5. If all these conditions are satisfied, the *PN fit* is considered satisfactory and only the fitting results for the R_j–C_j loop are reported. If one of these conditions is not satisfied, step 2 in the procedure is followed.
2. For each of the error metrics where *PN fit* is deemed unsatisfactory in step 1, the *full model fit* is compared to the *PN fit*. If the *full model fit* can improve one of the unsatisfactory error metrics from step 1 by at least 5%, the *full model fit* is used. If this is not the case, the *PN fit* is used, since the fitting quality is most likely affected by one or multiple outliers in the recorded impedance data.

The exact details used for both *PN fitting* and (ii) *full model fitting* are described in Appendices B.3 and B.4, respectively. Since the best-fit values resulting from CNLS analysis can be affected by the initial parameter estimates, the initial estimates and boundary conditions are included.

B.3. PN fit details

For *PN fitting*, the fit is performed with the following initial values:

- The R_j initial value is inherited from the experimentally obtained impedance data. More specifically, the magnitude at the lowest characterized frequency is used, which is the ratio between the amplitude of the voltage and current signal.
- The C_j initial value is 10 μF.

B.4. Full model fit details

For *full model fitting*, the following procedure is followed:

1. First, an initial PN junction fit is performed without the LH junction. The initial values are as follows:
   - The initial values for R_j and C_j are the same as in Appendix B.3.
   - The R_s initial value is inherited from the LOANA measurement in Table 2.
   - The L_s initial value is 100 nH.

   The values that are obtained through this initial fit are in the next step called $R_{s,init}$, $L_{s,init}$, $C_{j,init}$, and $R_{j,init}$.
2. Then, a fit is performed using all the circuit elements from Fig. 6 with the following initial values and boundary conditions:
   - The R_j initial value is $R_{j,init}$.
   - The C_j initial value is $C_{j,init}$.
   - The R_{LH} initial value is $0.02 \times R_{j,init}$
   - The C_{LH} initial value is $0.2 \times C_{j,init}$.
   - The R_s initial value is inherited from the LOANA measurement in Table 2. The upper and lower boundaries are $0.5 \times R_{s,LOANA}$ and $2 \times R_{s,LOANA}$.
   - The L_s initial value is 100 nH.

Appendix C. Best-fit circuit element values

The best-fit circuit element values and fitting errors from the procedure as described in Appendices A and B are presented for each of the characterized laminates in Table 4, 5, 6, 7, 8, 9, 10, and 11.

Table 5
Best-fit values for the Al-BSF-2 cell laminate.

V_{DC} (mV)	C_j (μF)	R_j (Ω)	C_{LH} (μF)	R_{LH} (Ω)	R_s (mΩ)	L_s (nH)	$NRMSE_M$ (–)	$RMSE_\theta$ (–)	$NRMSE_R$ (–)	$NRMSE_X$ (–)
0	9.046	988.4	–	–	–	–	0.0068	1.232	0.0071	0.0067
100	9.768	303.1	–	–	–	–	0.0058	1.755	0.0050	0.0177
200	10.61	87.91	–	–	–	–	0.0019	2.113	0.0020	0.0027
300	11.77	28.74	0.632	0.000	2.25	96.7	0.0018	2.238	0.0018	0.0072
350	12.65	16.10	1.988	0.000	2.25	96.1	0.0037	2.695	0.0037	0.0057
400	14.28	7.985	0.032	0.0050	2.32	91.3	0.0036	2.205	0.0037	0.0077
450	20.51	2.641	20.48	0.0299	2.25	84.3	0.0043	1.117	0.0045	0.0100
475	31.51	1.225	17.65	0.0394	2.25	84.7	0.0044	1.109	0.0046	0.0098
500	61.49	0.507	19.76	0.0348	4.74	89.7	0.0041	0.602	0.0042	0.0095
521[a]	124.6	0.230	0.902	0.0228	6.75	80.2	0.0051	0.720	0.0048	0.0076
525	146.5	0.194	0.0002	0.0210	6.89	81.2	0.0057	0.878	0.0054	0.0078
550	395.0	0.0740	0.0000	0.0139	7.24	85.9	0.0145	1.542	0.0158	0.0114
575	1318	0.0260	5.237	0.0081	8.95	88.2	0.0223	2.673	0.0499	0.0159

[a]Denotes the V_{DC} corresponding to the maximum power point.

Table 6
Best-fit values for the Al-BSF-3 cell laminate.

V_{DC} (mV)	C_j (μF)	R_j (Ω)	C_{LH} (μF)	R_{LH} (Ω)	R_s (mΩ)	L_s (nH)	$NRMSE_M$ (–)	$RMSE_\theta$ (–)	$NRMSE_R$ (–)	$NRMSE_X$ (–)
0	8.801	1434	–	–	–	–	0.0056	0.832	0.0026	0.0169
100	9.458	607.8	–	–	–	–	0.0035	0.982	0.0029	0.0143
200	10.33	172.9	–	–	–	–	0.0021	0.862	0.0020	0.0063
300	11.42	41.65	–	–	–	–	0.0041	0.955	0.0038	0.0054
350	12.23	18.42	–	–	–	–	0.0022	1.345	0.0023	0.0050
400	13.76	7.457	–	–	–	–	0.0042	2.170	0.0039	0.0090
450	19.70	2.265	19.67	0.0275	3.38	47.6	0.0046	2.441	0.0048	0.0095
475	30.57	1.057	30.03	0.0453	3.38	62.1	0.0043	1.086	0.0045	0.0097
500	59.99	0.444	30.53	0.0392	3.38	65.4	0.0044	0.663	0.0047	0.0100
506[a]	72.73	0.354	34.43	0.0333	5.77	64.5	0.0043	0.721	0.0044	0.0074
525	138.0	0.177	40.59	0.0216	6.44	64.2	0.0049	0.680	0.0047	0.0078
550	349.1	0.0691	69.59	0.0097	8.51	62.9	0.0086	0.854	0.0071	0.0073
575	947.1	0.0277	121.3	0.0046	8.74	62.4	0.0188	1.141	0.0155	0.0096

[a]Denotes the V_{DC} corresponding to the maximum power point.

Table 7
Best-fit values for the PERC cell laminate.

V_{DC} (mV)	C_j (μF)	R_j (Ω)	C_{LH} (μF)	R_{LH} (Ω)	R_s (mΩ)	L_s (nH)	$NRMSE_M$ (–)	$RMSE_\theta$ (–)	$NRMSE_R$ (–)	$NRMSE_X$ (–)
0	6.876	6384	–	–	–	–	0.0060	0.980	0.0118	0.0090
100	7.467	5155	–	–	–	–	0.0075	1.023	0.0123	0.0097
200	8.007	2002	–	–	–	–	0.0051	1.043	0.0048	0.0117
300	8.841	581.6	–	–	–	–	0.0052	1.210	0.0053	0.0062
350	9.321	262.5	–	–	–	–	0.0024	1.338	0.0024	0.0040
400	10.04	99.33	–	–	–	–	0.0017	1.607	0.0018	0.0058
450	11.88	29.18	0.0193	0.0076	2.19	56.2	0.0020	1.344	0.0020	0.0033
475	14.67	14.34	14.67	0.0356	2.17	49.0	0.0017	1.485	0.0018	0.0041
500	21.61	6.561	21.56	0.0647	2.17	70.1	0.0031	1.079	0.0031	0.0060
525	39.79	2.817	22.51	0.0548	8.66	70.5	0.0033	1.134	0.0034	0.0070
550	87.57	1.170	12.15	0.0341	6.75	64.1	0.0033	0.956	0.0033	0.0058
575	218.8	0.465	0.0085	0.0181	7.19	65.2	0.0040	1.712	0.0051	0.0059
587[a]	344.8	0.299	0.0061	0.0132	7.26	67.8	0.0053	2.385	0.0079	0.0071
600	577.2	0.183	0.0002	0.0096	7.18	68.9	0.0072	2.864	0.0122	0.0086
625	1594	0.0708	0.0445	0.0052	7.83	69.6	0.0141	3.220	0.0259	0.0109

[a]Denotes the V_{DC} corresponding to the maximum power point.

Table 8
Best-fit values for the TOPCon-1 cell laminate.

V_{DC} (mV)	C_j (μF)	R_j (Ω)	C_{LH} (μF)	R_{LH} (Ω)	R_s (mΩ)	L_s (nH)	$NRMSE_M$ (–)	$RMSE_\theta$ (–)	$NRMSE_R$ (–)	$NRMSE_X$ (–)
0	2.972	564.0	–	–	–	–	0.0042	0.606	0.0041	0.0046
100	3.222	525.9	–	–	–	–	0.0020	0.656	0.0022	0.0095
200	3.536	415.9	–	–	–	–	0.0055	0.579	0.0055	0.0034
300	3.982	233.2	–	–	–	–	0.0064	0.572	0.0064	0.0068
350	4.367	142.9	–	–	–	–	0.0048	0.569	0.0047	0.0073
400	5.456	72.81	–	–	–	–	0.0059	1.573	0.0059	0.0048
450	11.29	26.70	11.240	0.269	2.86	70.5	0.0019	1.233	0.0019	0.0089

(*continued on next page*)

Table 8 (*continued*).

V_{DC} (mV)	C_j (μF)	R_j (Ω)	C_{LH} (μF)	R_{LH} (Ω)	R_s (mΩ)	L_s (nH)	$NRMSE_M$ (–)	$RMSE_\theta$ (–)	$NRMSE_R$ (–)	$NRMSE_X$ (–)
475	18.25	16.02	12.206	0.222	2.86	81.5	0.0016	0.812	0.0016	0.0068
500	41.25	7.577	15.810	0.121	8.11	82.9	0.0028	0.785	0.0028	0.0041
525	101.9	3.376	28.73	0.0502	11.4	79.4	0.0010	0.889	0.0012	0.0022
550	268.2	1.426	35.28	0.0225	7.16	75.1	0.0010	0.830	0.0011	0.0019
575	714.3	0.585	0.0072	0.0104	6.32	66.0	0.0012	0.956	0.0013	0.0021
589[a]	1228	0.353	5.798	0.0067	6.80	67.1	0.0020	1.267	0.0021	0.0028
600	1857	0.238	0.928	0.0062	5.54	67.3	0.0028	1.433	0.0028	0.0036
625	4557	0.0964	48.10	0.0055	4.18	69.1	0.0058	1.820	0.0060	0.0053

[a]Denotes the V_{DC} corresponding to the maximum power point.

Table 9
Best-fit values for the TOPCon-2 cell laminate.

V_{DC} (mV)	C_j (μF)	R_j (Ω)	C_{LH} (μF)	R_{LH} (Ω)	R_s (mΩ)	L_s (nH)	$NRMSE_M$ (–)	$RMSE_\theta$ (–)	$NRMSE_R$ (–)	$NRMSE_X$ (–)
0	4.131	3224	–	–	–	–	0.0112	1.020	0.0109	0.0120
100	4.405	1121	–	–	–	–	0.0042	0.918	0.0052	0.0069
200	4.764	311.6	–	–	–	–	0.0042	0.700	0.0040	0.0132
300	5.183	55.45	–	–	–	–	0.0026	0.584	0.0027	0.0043
350	5.568	23.26	–	–	–	–	0.0031	0.669	0.0030	0.0064
400	6.314	9.989	–	–	–	–	0.0041	1.054	0.0044	0.0084
450	9.66	4.382	6.561	0.134	2.59	56.1	0.0087	6.418	0.0101	0.0190
475	17.63	2.784	15.23	0.336	10.2	65.3	0.0040	0.754	0.0041	0.0085
500	33.82	1.902	15.44	0.224	10.3	73.6	0.0038	1.106	0.0041	0.0084
525	72.95	1.290	21.04	0.114	10.3	77.2	0.0033	1.073	0.0035	0.0074
550	173.9	0.797	35.41	0.0480	10.3	73.3	0.0027	1.235	0.0029	0.0054
575	438.1	0.435	48.62	0.0203	8.09	66.5	0.0024	0.815	0.0024	0.0045
587[a]	689.9	0.312	43.66	0.0154	6.03	64.1	0.0029	1.057	0.0027	0.0046
600	1137	0.212	44.00	0.0100	6.72	61.9	0.0047	1.723	0.0046	0.0061
625	2984	0.0950	0.105	0.0049	7.09	60.7	0.0111	2.726	0.0107	0.0103

[a]Denotes the V_{DC} corresponding to the maximum power point.

Table 10
Best-fit values for the IBC cell laminate.

V_{DC} (mV)	C_j (μF)	R_j (Ω)	C_{LH} (μF)	R_{LH} (Ω)	R_s (mΩ)	L_s (nH)	$NRMSE_M$ (–)	$RMSE_\theta$ (–)	$NRMSE_R$ (–)	$NRMSE_X$ (–)
0	1.128	95.46	–	–	–	–	0.0031	0.854	0.0033	0.0067
100	1.229	98.17	–	–	–	–	0.0032	0.812	0.0032	0.0059
200	1.371	89.77	–	–	–	–	0.0023	0.755	0.0021	0.0064
300	1.692	65.44	–	–	–	–	0.0039	0.729	0.0036	0.0071
350	2.490	43.12	–	–	–	–	0.0045	3.348	0.0069	0.0098
400	7.890	18.70	4.092	0.450	2.79	137.6	0.0021	1.802	0.0023	0.0042
450	44.94	5.582	16.00	0.105	11.1	122.9	0.0014	1.441	0.0013	0.0029
475	113.1	2.823	36.02	0.0418	11.1	112.0	0.0010	1.404	0.0011	0.0018
500	277.9	1.396	102.8	0.0158	11.1	105.9	0.0008	0.978	0.0009	0.0014
525	638.1	0.695	113.9	0.0100	6.26	104.5	0.0006	0.802	0.0006	0.0011
550	1327	0.349	173.5	0.0064	5.53	102.8	0.0009	0.724	0.0010	0.0014
566[a]	2019	0.223	274.5	0.0046	5.79	102.1	0.0014	0.883	0.0017	0.0018
575	2513	0.173	291.1	0.0043	5.46	101.9	0.0018	0.969	0.0023	0.0020
600	4430	0.0842	425.8	0.0035	5.11	101.2	0.0038	1.174	0.0047	0.0028
625	7751	0.0386	431.4	0.0037	4.24	101.6	0.0048	1.267	0.0097	0.0035

[a]Denotes the V_{DC} corresponding to the maximum power point.

Table 11
Best-fit values for the SHJ cell laminate.

V_{DC} (mV)	C_j (μF)	R_j (Ω)	C_{LH} (μF)	R_{LH} (Ω)	R_s (mΩ)	L_s (nH)	$NRMSE_M$ (–)	$RMSE_\theta$ (–)	$NRMSE_R$ (–)	$NRMSE_X$ (–)
0	6.976	353.7	–	–	–	–	0.0036	0.756	0.0035	0.0154
100	7.628	334.3	–	–	–	–	0.0039	0.756	0.0042	0.0082
200	8.402	268.2	–	–	–	–	0.0032	0.964	0.0034	0.0163
300	9.547	143.5	–	–	–	–	0.0042	1.199	0.0043	0.0058
350	10.44	84.48	–	–	–	–	0.0032	1.652	0.0032	0.0051
400	12.50	46.36	–	–	–	–	0.0022	3.398	0.0024	0.0063
450	22.10	23.29	22.06	0.0906	1.92	107.9	0.0007	3.131	0.0008	0.0029
475	39.16	15.82	30.09	0.0880	7.68	111.9	0.0010	1.007	0.0009	0.0033
500	83.42	10.24	32.39	0.0535	7.68	111.7	0.0009	1.136	0.0009	0.0013
525	200.1	6.257	42.21	0.0289	7.68	110.9	0.0012	1.330	0.0011	0.0022
550	514.0	3.492	29.62	0.0144	6.23	101.7	0.0010	1.483	0.0009	0.0018
575	1347	1.782	0.0001	0.0062	7.17	97.7	0.0009	2.153	0.0009	0.0019
600	3411	0.860	2.912	0.0034	6.97	99.1	0.0012	3.328	0.0015	0.0021
625	8052	0.403	8.594	0.0017	7.21	99.5	0.0025	3.269	0.0032	0.0037
636[a]	11147	0.284	2.406	0.0015	7.37	99.7	0.0064	3.644	0.0086	0.0079
650	17574	0.180	55.75	0.0017	6.84	99.9	0.0072	3.691	0.0086	0.0058
675	35205	0.0740	0.370	0.0016	6.75	99.9	0.0127	3.906	0.0169	0.0085

[a]Denotes the V_{DC} corresponding to the maximum power point.

Appendix D. Supplementary data

Supplementary material related to this article can be found online at https://doi.org/10.1016/j.solmat.2023.112486.

References

[1] Fraunhofer ISE, Photovoltaics Report, 2023, https://www.ise.fraunhofer.de/en/publications/studies/photovoltaics-report.html. (Last Accessed on 31 March 2023).

[2] H. Ziar, P. Manganiello, O. Isabella, M. Zeman, Photovoltatronics: intelligent PV-based devices for energy and information applications, Energy Environ. Sci. 14 (2021) 106–126.

[3] S.M. MacAlpine, R.W. Erickson, M.J. Brandemuehl, Characterization of power optimizer potential to increase energy capture in photovoltaic systems operating under nonuniform conditions, IEEE Trans. Power Electron. (2013).

[4] A. Calcabrini, R. Weegink, P. Manganiello, M. Zeman, O. Isabella, Simulation study of the electrical yield of various PV module topologies in partially shaded urban scenarios, Sol. Energy 225 (2021) 726–733.

[5] C. Deline, B. Sekulic, J. Stein, S. Barkaszi, J. Yang, S. Kahn, Evaluation of maxim module-integrated electronics at the DOE regional test centers, in: 2014 IEEE 40th Photovoltaic Specialist Conference, PVSC, 2014, pp. 0986–0991, http://dx.doi.org/10.1109/PVSC.2014.6925080.

[6] S.Z.M. Golroodbari, A.C.D. Waal, W.G.J.H.M.V. Sark, Improvement of shade resilience in photovoltaic modules using buck converters in a smart module architecture, Energies 11 (1) (2018).

[7] J.T. Stauth, M.D. Seeman, K. Kesarwani, A resonant switched-capacitor IC and embedded system for sub-module photovoltaic power management, IEEE J. Solid-State Circuits 47 (12) (2012) 3043–3054.

[8] J. Panigrahi, Vandana, R. Singh, N. Batra, J. Gope, M. Sharma, P. Pathi, S. Srivastava, C. Rauthan, P. Singh, Impedance spectroscopy of crystalline silicon solar cell: Observation of negative capacitance, Sol. Energy 136 (2016) 412–420.

[9] A.H. Chang, A.-T. Avestruz, S.B. Leeb, Capacitor-less photovoltaic cell-level power balancing using diffusion charge redistribution, IEEE Trans. Power Electron. 30 (2) (2015) 537–546.

[10] R. Ayop, C.W. Tan, Design of boost converter based on maximum power point resistance for photovoltaic applications, Sol. Energy 160 (2018) 322–335.

[11] D.A. van Nijen, P. Manganiello, M. Zeman, O. Isabella, Exploring the benefits, challenges, and feasibility of integrating power electronics into c-si solar cells, Cell Rep. Phys. Sci. 3 (7) (2022) 100944.

[12] S. Rahimpour, H. Tarzamni, N.V. Kurdkandi, O. Husev, D. Vinnikov, F. Tahami, An overview of lifetime management of power electronic converters, IEEE Access 10 (2022) 109688–109711.

[13] J.-H. Huang, B. Lehman, T. Qian, Submodule integrated boost DC-DC converters with no external input capacitor or input inductor for low power photovoltaic applications, in: 2016 IEEE Energy Conversion Congress and Exposition, ECCE, 2016, pp. 1–7, http://dx.doi.org/10.1109/ECCE.2016.7855476.

[14] E. von Hauff, Impedance spectroscopy for emerging photovoltaics, J. Phys. Chem. C 123 (18) (2019) 11329–11346.

[15] M. Suresh, Measurement of solar cell parameters using impedance spectroscopy, Sol. Energy Mater. Sol. Cells 43 (1) (1996) 21–28.

[16] R.A. Kumar, M.S. Suresh, J. Nagaraju, Facility to measure solar cell ac parameters using an impedance spectroscopy technique, Rev. Sci. Instrum. 72 (8) (2001) 3422–3426.

[17] R.A. Kumar, M. Suresh, J. Nagaraju, Silicon (BSFR) solar cell AC parameters at different temperatures, Sol. Energy Mater. Sol. Cells 85 (3) (2005) 397–406.

[18] S. Kumar, P. Singh, G. Chilana, Study of silicon solar cell at different intensities of illumination and wavelengths using impedance spectroscopy, Sol. Energy Mater. Sol. Cells 93 (10) (2009) 1881–1884.

[19] I. Mora-Seró, G. Garcia-Belmonte, P.P. Boix, M.A. Vázquez, J. Bisquert, Impedance spectroscopy characterisation of highly efficient silicon solar cells under different light illumination intensities, Energy Environ. Sci. 2 (2009) 678–686.

[20] J.E. Garland, D.J. Crain, J.P. Zheng, C.M. Sulyma, D. Roy, Electro-analytical characterization of photovoltaic cells by combining voltammetry and impedance spectroscopy: voltage dependent parameters of a silicon solar cell under controlled illumination and temperature, Energy Environ. Sci. 4 (2011) 485–498.

[21] P. Yadav, B. Tripathi, K. Pandey, M. Kumar, Investigating the charge transport kinetics in poly-crystalline silicon solar cells for low-concentration illumination by impedance spectroscopy, Sol. Energy Mater. Sol. Cells 133 (2015) 105–112.

[22] A. Blank, N. Suhareva, Admittance spectra of silicon photocells in dark mode, Sensors Actuators A 331 (2021) 112909.

[23] M.M. Shehata, T.N. Truong, R. Basnet, H.T. Nguyen, D.H. Macdonald, L.E. Black, Impedance spectroscopy characterization of c-Si solar cells with SiO_x/ poly-Si rear passivating contacts, Sol. Energy Mater. Sol. Cells 251 (2023) 112167.

[24] O.I. Olayiwola, P.S. Barendse, Characterization of silicon-based photovoltaic cells using broadband impedance spectroscopy, IEEE Trans. Ind. Appl. 54 (6) (2018) 6309–6319.

[25] T. Yeow, J. Sun, Z. Yao, J.-N. Jaubert, K.P. Musselman, Evaluation of impedance spectroscopy as a tool to characterize degradation mechanisms in silicon photovoltaics, Sol. Energy 184 (2019) 52–58.

[26] O.I. Olayiwola, P.S. Barendse, Photovoltaic cell/module equivalent electric circuit modeling using impedance spectroscopy, IEEE Trans. Ind. Appl. 56 (2) (2020) 1690–1701.

[27] R.A. Guejia-Burbano, G. Petrone, M. Piliougine, Impedance spectroscopy for diagnosis of photovoltaic modules under outdoor conditions, IEEE J. Photovolt. 12 (6) (2022) 1503–1512.

[28] M. Pravettoni, D. Poh, J.P. Singh, J.W. Ho, K. Nakayashiki, The effect of capacitance on high-efficiency photovoltaic modules: a review of testing methods and related uncertainties, J. Phys. D: Appl. Phys. 54 (2021) 193001.

[29] P. tools, LOANA solar cell analysis system, 2022, http://www.pv-tools.de/products/loana-system/loana-start.html. (Last Accessed on 21 December 2022).

[30] D.A. Neamen, Semiconductor Physics and Devices, fourth ed., McGraw Hill Education, 2012.

[31] M.L. Lucia, J.L. Hernandez-Rojas, C. Leon, I. Mártil, Capacitance measurements of p-n junctions: depletion layer and diffusion capacitance contributions, Eur. J. Phys. 14 (2) (1993) 86.

[32] T.G. Allen, J. Bullock, X. Yang, A. Javey, S.D. Wolf, Passivating contacts for crystalline silicon solar cells, Nat. Energy 4 (11) (2019) 914–928.

[33] H. Steinkemper, M. Hermle, S.W. Glunz, Comprehensive simulation study of industrially relevant silicon solar cell architectures for an optimal material parameter choice, Prog. Photovolt., Res. Appl. 24 (10) (2016) 1319–1331.

[34] Y. Liu, Y. Li, Y. Wu, G. Yang, L. Mazzarella, P. Procel-Moya, A.C. Tamboli, K. Weber, M. Boccard, O. Isabella, X. Yang, B. Sun, High-efficiency silicon heterojunction solar cells: Materials, devices and applications, Mater. Sci. Eng. R 142 (2020) 100579.

[35] L. Cao, P. Procel, A. Alcañiz, J. Yan, F. Tichelaar, E. Özkol, Y. Zhao, C. Han, G. Yang, Z. Yao, M. Zeman, R. Santbergen, L. Mazzarella, O. Isabella, Achieving 23.83% conversion efficiency in silicon heterojunction solar cell with ultra-thin MoO_x hole collector layer via tailoring (i)a-Si: H/MoO_x interface, Prog. Photovolt., Res. Appl. (2022).

[36] M. Bivour, C. Messmer, L. Neusel, F. Zähringer, J.S. nad S.W. Glunz, M. Hermle, Principles of carrier-selective contacts based on induced junctions, in: 33rd European Photovoltaic Solar Energy Conference and Exhibition, 2017, pp. 348–352, http://dx.doi.org/10.4229/EUPVSEC20172017-2BO.4.2.

[37] O. von Roos, A simple theory of back surface field (BSF) solar cells, J. Appl. Phys. 49 (6) (1978) 3503–3511.

[38] O. Breitenstein, J.P. Rakotoniaina, M.H. Al Rifai, M. Werner, Shunt types in crystalline silicon solar cells, Prog. Photovolt., Res. Appl. 12 (7) (2004) 529–538.

[39] B.A. Boukamp, A nonlinear least squares fit procedure for analysis of immittance data of electrochemical systems, Solid State Ion. 20 (1) (1986) 31–44.

[40] A. Smets, K. Jäger, O. Isabella, R. van Swaaij, M. Zeman, Solar Energy - the Physics and Engineering of Photovoltaic Conversion Technologies and Systems, 2016.

[41] P. Procel, P. Löper, F. Crupi, C. Ballif, A. Ingenito, Numerical simulations of hole carrier selective contacts in p-type c-si solar cells, Sol. Energy Mater. Sol. Cells 200 (2019) 109937.

[42] P. Procel, G. Yang, O. Isabella, M. Zeman, Theoretical evaluation of contact stack for high efficiency IBC-SHJ solar cells, Sol. Energy Mater. Sol. Cells 186 (2018) 66–77.

[43] P. Procel, H. Xu, A. Saez, C. Ruiz-Tobon, L. Mazzarella, Y. Zhao, C. Han, G. Yang, M. Zeman, O. Isabella, The role of heterointerfaces and subgap energy states on transport mechanisms in silicon heterojunction solar cells, Prog. Photovolt., Res. Appl. 28 (9) (2020) 935–945.

[44] N. Jensen, U. Rau, R.M. Hausner, S. Uppal, L. Oberbeck, R.B. Bergmann, J.H. Werner, Recombination mechanisms in amorphous silicon/crystalline silicon heterojunction solar cells, J. Appl. Phys. 87 (5) (2000) 2639–2645.

[45] Y. Chen, D. Chen, C. Liu, Z. Wang, Y. Zou, Y. He, Y. Wang, L. Yuan, J. Gong, W. Lin, X. Zhang, Y. Yang, H. Shen, Z. Feng, P.P. Altermatt, P.J. Verlinden, Mass production of industrial tunnel oxide passivated contacts (i-topcon) silicon solar cells with average efficiency over 23% and modules over 345 w, Prog. Photovolt., Res. Appl. 27 (10) (2019) 827–834.

[46] J. Veirman, R. Varache, M. Albaric, A. Danel, B. Guo, N. Fu, Y. Wang, Silicon wafers for industrial n-type SHJ solar cells: Bulk quality requirements, large-scale availability and guidelines for future developments, Sol. Energy Mater. Sol. Cells 228 (2021) 111128.

[47] J. Haschke, O. Dupré, M. Boccard, C. Ballif, Silicon heterojunction solar cells: Recent technological development and practical aspects - from lab to industry, Sol. Energy Mater. Sol. Cells 187 (2018) 140–153.

[48] C. Ballif, F.-J. Haug, M. Boccard, P.J. Verlinden, G. Hahn, Status and perspectives of crystalline silicon photovoltaics in research and industry, Nat. Rev. Mater. (2022).

[49] B. Steinhauser, T. Niewelt, A. Richter, R. Eberle, M.C. Schubert, Extraordinarily high minority charge carrier lifetime observed in crystalline silicon, Solar RRL 5 (11) (2021) 2100605.

[50] A. Descoeudres, C. Allebé, N. Badel, L. Barraud, J. Champliaud, G. Christmann, F. Debrot, A. Faes, J. Geissbühler, J. Horzel, A. Lachowicz, J. Levrat, S. Martin de Nicolas, S. Nicolay, B. Paviet-Salomon, L.-L. Senaud, C. Ballif, M. Despeisse, Low-temperature processes for passivation and metallization of high-efficiency crystalline silicon solar cells, Sol. Energy 175 (2018) 54–59, Recent Progress in Photovoltaics, Part 1.

[51] A. Descoeudres, J. Horzel, B. Paviet-Salomon, L.-L. Senaud, G. Christmann, J. Geissbühler, P. Wyss, N. Badel, J.-W. Schüttauf, J. Zhao, C. Allebé, A. Faes, S. Nicolay, C. Ballif, M. Despeisse, The versatility of passivating carrier-selective silicon thin films for diverse high-efficiency screen-printed heterojunction-based solar cells, Prog. Photovolt., Res. Appl. 28 (6) (2020) 569–577.

[52] T. Niewelt, A. Richter, T. Kho, N. Grant, R. Bonilla, B. Steinhauser, J.-I. Polzin, F. Feldmann, M. Hermle, J. Murphy, S. Phang, W. Kwapil, M. Schubert, Taking monocrystalline silicon to the ultimate lifetime limit, Sol. Energy Mater. Sol. Cells 185 (2018) 252–259.

[53] A. Richter, M. Hermle, S.W. Glunz, Reassessment of the limiting efficiency for crystalline silicon solar cells, IEEE J. Photovolt. 3 (4) (2013) 1184–1191.

[54] M.J. Kerr, A. Cuevas, P. Campbell, Limiting efficiency of crystalline silicon solar cells due to Coulomb-enhanced auger recombination, Prog. Photovolt., Res. Appl. 11 (2) (2003) 97–104.

[55] M.J. Kerr, A. Cuevas, General parameterization of auger recombination in crystalline silicon, J. Appl. Phys. 91 (4) (2002) 2473–2480.

[56] A. Richter, S.W. Glunz, F. Werner, J. Schmidt, A. Cuevas, Improved quantitative description of auger recombination in crystalline silicon, Phys. Rev. B 86 (2012) 165202.

[57] E.B. Rosa, The self and mutual inductances of linear conductors, Bull. Bureau Standards 4 (1908) 301–344.

[58] K.C. Fong, K.R. McIntosh, A.W. Blakers, Accurate series resistance measurement of solar cells, Prog. Photovolt., Res. Appl. 21 (4) (2013) 490–499.